Journal of Materials Chemistry

Cite this: J. Mater. Chem., 2011, 21, 6313

www.rsc.org/materials

PAPER

$Zn_3V_2O_7(OH)_2(H_2O)_2$ and $Zn_3V_2O_8$ nanostructures: controlled fabrication and photocatalytic performance†

Rui Shi,[a] Yajun Wang,[a] Feng Zhou[b] and Yongfa Zhu*[a]

Received 20th December 2010, Accepted 22nd February 2011
DOI: 10.1039/c0jm04451b

Floriated like and nanobelt nanostructures of $Zn_3V_2O_7(OH)_2(H_2O)_2$ were successfully synthesized by a template-free hydrothermal route. The as-prepared floriated nanostructures were composed of 2D nanosheets, which intercrossed with each other through self-assembly. The influence of the hydrothermal temperature on the morphology and photocatalytic activities of products was systematically investigated. Significantly, this is the first time that $Zn_3V_2O_7(OH)_2(H_2O)_2$ was used as a photocatalyst for organic pollutant degradation under UV light irradiation. Moreover, $Zn_3V_2O_8$ with porous nanostructures could be formed *via* calcination of the corresponding $Zn_3V_2O_7(OH)_2(H_2O)_2$. It was found that the $Zn_3V_2O_8$ nanostructure still possessed floriated like morphology and the pore sizes within the floriated were about 4 nm. All these characteristics were beneficial for the improvement of photocatalytic activity. The reaction constant (k) of the best quality $Zn_3V_2O_8$ nanostructure was three times that of the sample prepared by solid-state reaction under visible-light irradiation.

Introduction

Semiconductor photocatalytic degradation had been widely applied as a technique for the destruction of organic pollutants in wastewater.[1,2] Representative examples are TiO_2-based photocatalytic detoxification of water for environmental remediation.[3] However, the overall efficiency of TiO_2 is still low for commercial use, due to its poor match to the solar spectrum owing to a wide band gap energy.[4–6] Anion-doping with N, C, and S or cation-doping with transition metals are commonly used to functionalize TiO_2 as a visible-light photocatalyst.[7–11] Another effective method is to develop novel visible-light responsive photocatalysts.[12–16]

According to a previous theoretical study, the V 3d orbital is usually located below the analogous d orbitals of the other transition metals in the energy spectrum and lowers the bottom conduction band to a more positive position.[17] Accordingly, vanadium is considered to be an important candidate element as visible-light photocatalyst. Some vanadium-containing oxides, such as $BiVO_4$ and $InVO_4$, had been developed successfully as visible-light photocatalysts for O_2 and H_2 evolution in the presence of sacrificial reagents $AgNO_3$ or CH_3OH, respectively.[18–20] Recently, Wang and his co-workers found $Zn_3V_2O_8$ had photocatalytic activity for O_2 evolution under visible light irradiation.[21] Their work revealed that $Zn_3V_2O_8$ could perform as excellent photocatalytic material and solar energy transfer material. However, the $Zn_3V_2O_8$ sample was prepared by solid-state reaction in their work, and the photocatalytic activity was not high. For commercial application as photocatalyst, a material must have superior photocatalytic activity, and also be easily prepared. It is well known that conventional solid-state reactions are not only characterized by high energy consumption but also result in the formation of photocatalysts with low surface areas.[22] And low surface will lead to low photocatalytic activity. Nanostructured photocatalysts usually have high photocatalytic activities because of their special morphologies, high surface areas and high efficiency of electron-hole separation.[23] Therefore, this inspired us to synthesize nanostructured $Zn_3V_2O_8$ through soft chemical methods.

It has been well-known that low-dimension nanostructures have unique optical, magnetic, and catalytic properties and are expected to be elementary units of optoelectronic devices.[24,25] The synthesis of low-dimension nanostructures and guiding of these nanometer-scaled building blocks to ordered superstructures of complex functional architectures would offer great opportunities to explore their novel properties and lead to the construction of nanoscale devices. For example, the flower-like superstructure Bi_2WO_6 exhibits much higher photocatalytic efficiency due to a high adsorption percentage of organic dye and penetration of visible-light wave which leads to high charge mobility.[26] Another typical example is that the hierarchical architecture of ZnS leads to higher photocatalytic activity. The rough surfaces of the hierarchical architecture with increased area and permeability could provide ideal activity sites for photocatalytic reactions.[27] Therefore, the development of facile,

[a]Department of Chemistry, Tsinghua University, Beijing, 100084, China. E-mail: zhuyf@tsinghua.edu.cn; Fax: +86-10-62787601; Tel: +86-10-62787601
[b]Department of Materials Science and Engineering, Dalian Maritime University, Dalian, 116026, P. R. China

† Electronic supplementary information (ESI) available: Fig. S1–S9 and Table S1. See DOI: 10.1039/c0jm04451b

template-free, and self-assembly routes for the formation of hierarchical nanostructures is of great interest. Herein, for the first time, we successfully synthesized hierarchical nanostructure $Zn_3V_2O_7(OH)_2(H_2O)_2$ with floriated like and nanobelt morphologies *via* a template-free hydrothermal route and then converted the $Zn_3V_2O_7(OH)_2(H_2O)_2$ precursors into porous $Zn_3V_2O_8$ with similar nanostructure by calcination treatment. It was found that the photocatalytic activities were significantly improved when the $Zn_3V_2O_8$ was shaped as a flower-like superstructure. Moreover, for the first time, we report that these two $Zn_3V_2O_7(OH)_2(H_2O)_2$ morphologies show quite different activities in organic pollutant degradation.

Experimental section

Synthesis of $Zn_3V_2O_7(OH)_2(H_2O)_2$

$Zn_3V_2O_7(OH)_2(H_2O)_2$ with different morphologies was synthesized *via* a simple hydrothermal process. All chemicals used were analytic grade reagents used without further purification. For the synthesis of floriated like and nanobelt nanostructures, Zn $(NO_3)_2$ and $NaVO_3$ (3 : 2 molar ratio) were mixed together, and then a yellow suspension appeared immediately. This suspension was added into a 40 mL Teflon-lined autoclave and filled with deionized water up to 80% of the total volume. After that, the autoclave was sealed into a stainless steel tank and kept at a temperature range from 60 to 140 °C for 20 h. Then the reactor was cooled to room-temperature naturally. The resulting sample was collected and washed with deionized water and dried at 60 °C in air.

Synthesis of $Zn_3V_2O_8$

To get the $Zn_3V_2O_8$ products, the hydrothermally synthesized $Zn_3V_2O_7(OH)_2(H_2O)_2$ heated at 70 °C was first dried in air and then directly calcined in a furnace at different calcination temperatures for 1 h in air without any other treatment. Meanwhile $Zn_3V_2O_8$ was synthesized by traditional solid-state reaction according to the literature for comparison with the nanostructure.[21]

Characterization

The purity and crystallinity of the as-prepared sample was characterized by XRD on Bruker D8-advance diffractometer using CuKα radiation (λ = 1.5418 Å). The XRD data for indexing and cell-parameter calculations were collected in a scanning mode with a step length of 0.02° and a preset time of 5.6 s/step. Morphologies and structures of the as-prepared samples were characterized by scanning electron micrographs (SEM KYKY-2800) and transmission electron microscopy (HRTEM JEOL JEM 2010). Thermogravimetric analysis (TGA) and differential thermal analysis (DTA) were performed on a Dupont 1090 thermal analyzer, the atmosphere was air, and the heating rate was 5 °C min^{-1}. The Brunauer-Emmett-Teller (BET) surface area and porosity was monitored by ASAP 2010 V5.02H. Total organic carbon (TOC) was measured with a Tekmar Dohrmann Apollo 9000 TOC analyzer. UV-vis diffuse reflectance spectra (DRS) of the samples were measured by using a Hitachi U-3010 UV-vis spectrophotometer.

Photocatalytic tests

The photocatalytic activities of the $Zn_3V_2O_7(OH)_2(H_2O)_2$ and $Zn_3V_2O_8$ were evaluated by degradation of MB under 11-W bactericidal lamp with a 254 nm and 500 W Xe lamp with a 420 nm cutoff filter, respectively. The average light intensity was 0.8 and 28 mW cm^{-2}, respectively, for the bactericidal lamp and the Xe lamp. The reaction cell was placed in a sealed black box of which the top was opened under UV light irradiation or the 420 nm cutoff filters were placed to provide visible light irradiation. In each run, 50 mg of the catalyst was added to 100 mL of the MB solution (1.0×10^{-5} mol L^{-1}). After the suspension was stirred for 30 min, the light was turned on to initiate the reaction. The concentration of the MB solution was monitored using a Hitachi UV-vis spectrophotometer. To identify reaction intermediates, the original concentration of MB was increased to 5.0×10^{-5} mol L^{-1}. HPLC monitoring was carried out using a UV absorbance detector operated at 280 nm coupled to a Venusil XBP-C18 column. The intermediates were finally identified by LC/MS (Thermo Fisher, LTQ).

Results and discussion

Structure of $Zn_3V_2O_7(OH)_2(H_2O)_2$

The hydrothermal temperature greatly influenced the structure and growth of $Zn_3V_2O_7(OH)_2(H_2O)_2$. Fig. 1 showed the X-ray diffraction (XRD) patterns of samples prepared at different hydrothermal temperatures. When the reactant was maintained at 60 °C for 20 h, several peaks were observed. These peaks can be attributed to the hexagonal structure of $Zn_3V_2O_7(OH)_2(H_2O)_2$, based on standard diffraction patterns of $Zn_3V_2O_7(OH)_2(H_2O)_2$ (JCPDS Card number:87-0417). In the temperature range of 60–90 °C, the shape of diffraction peaks became more clean-cut and intensities increased gradually, indicating better nanocrystallines formed. At the top of Fig. 1, a standard XRD pattern of $Zn_3V_2O_7(OH)_2(H_2O)_2$ is given. The standard intensity of the (001) peak was about 3 and 20 times that of the (102) and (110) peaks, which could be expressed as $I_{(001)}/I_{(102)} = 3$ and $I_{(001)}/I_{(110)} = 20$. However, in the temperature series samples the value of $I_{(001)}/I_{(102)}$ and $I_{(001)}/I_{(110)}$ were almost smaller than 1.5 and 6 below 90 °C. This implied that the crystal had special anisotropic growth along the [102] and [110] directions.[23,28] Moreover, in the

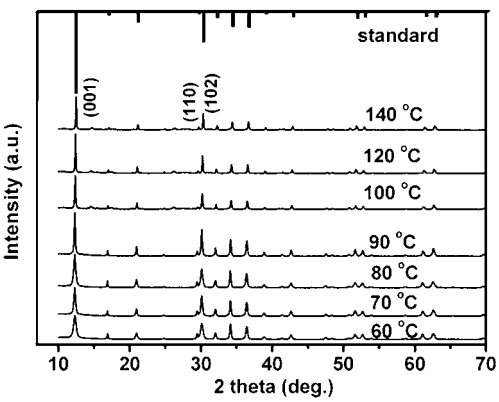

Fig. 1 XRD patterns of series $Zn_3V_2O_7(OH)_2(H_2O)_2$ prepared at different hydrothermal temperatures.

temperature range 100–140 °C, the intensities of the (102) and (110) diffraction peaks started to change, indicating the growth direction of samples changed again. These conclusions could be further confirmed by HRTEM observation below.

Photophysical properties of $Zn_3V_2O_7(OH)_2(H_2O)_2$

UV-vis spectra of the as-prepared samples are shown in Fig. 2. It is note-worthy that the onsets of the samples were strongly dependent on the hydrothermal temperature. When the temperature was lower than 80 °C, the samples showed the same absorption onset in the UV light region. The steep shape of the spectra indicated that the absorption was not due to the transition from the impurity level but was due to the band-gap transition,[29] and energy band gap estimated from the absorption edge was 3.25 eV. However, the absorption onsets of the samples were red-shifted apparently, when the temperature increased from 90 to 140 °C. In addition, an apparent absorption edge with an extrapolated absorption edge at ~680 nm (~1.79 eV) was observed. Generally speaking, during the reaction at a higher temperature, it is easier for oxygen vacancies to form in the structure; consequently, in our work, the optical absorption properties of the $Zn_3V_2O_7(OH)_2(H_2O)_2$ prepared at higher hydrothermal temperature is greatly influenced by oxygen vacancies, and the extrapolated absorption at about 680 nm could be attributed to oxygen vacancies.[30,31] Hence, the color of the samples turned from white to red during the reaction in the temperature range from 60 to 140 °C, as can be expected from the absorption spectrum.

Morphology of $Zn_3V_2O_7(OH)_2(H_2O)_2$

The morphologies of the final products were characterized by SEM and TEM. The low-magnification SEM image (Fig. 3a) of the product obtained at 60 °C shows that $Zn_3V_2O_7(OH)_2(H_2O)_2$ was basically composed of floriated nanostructures with an average diameter of about 1 μm. The magnified image in Fig. 3b clearly demonstrates the surface structure of the floriated like morphology, from which one can see that dozens of 2D nanosheets (with a side length of about 500 nm and a thickness of about 10 nm) are intercrossed with each other and have formed floriated microspheres through self-assembly. The detailed crystal structure and morphology of the floriated sample can be

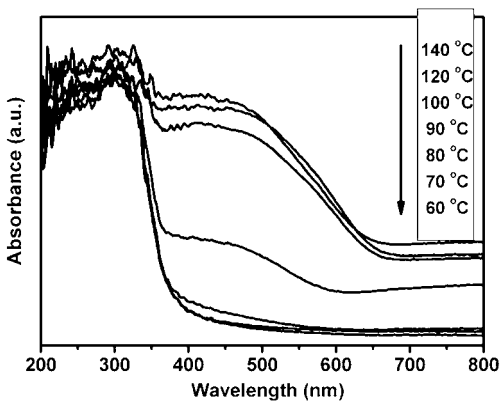

Fig. 2 UV-vis spectra of series $Zn_3V_2O_7(OH)_2(H_2O)_2$ prepared at different hydrothermal temperatures.

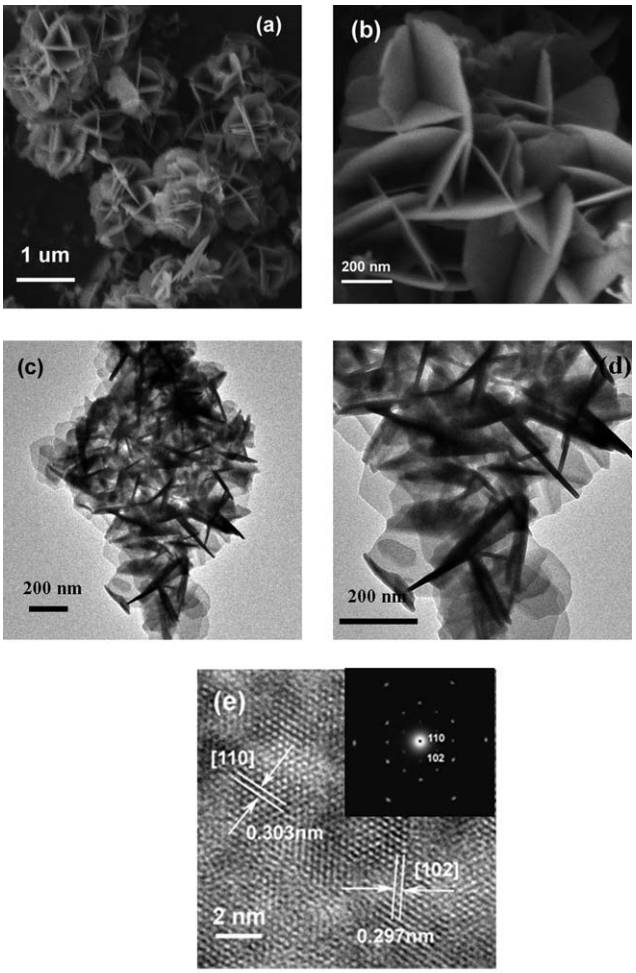

Fig. 3 SEM images (a, b), TEM images (c, d), HRTEM image (e) and SAED pattern (upper inset in Figure 3e) of $Zn_3V_2O_7(OH)_2(H_2O)_2$ prepared at 60 °C.

further observed by TEM. It can be seen from Fig. 3c and 3d that the difference in electron density between the dark edge and pale sheet clearly confirms the presence of the floriated nanostructures fabricated with nanosheets, which corresponds well with the SEM images. The high crystallinity of the present product can be obviously observed from the HRTEM image in Fig. 3e. The regular spacings of the observed lattice planes were 0.303 and 0.297 nm, which correspond to the (110) and (102) plane of hexagonal $Zn_3V_2O_7(OH)_2(H_2O)_2$, respectively. Moreover, at the corner of Fig. 3e, the corresponding selective area electron diffraction (SAED) pattern with a regular and clear hexagonal diffraction spot array revealed the single-crystal nature of the nanosheet. Further studies of the SAED and HRTEM image demonstrated that the nanosheet grew preferentially along the [110] and [102] direction, which was consistent with the XRD results. When the hydrothermal temperature was increased to 70 or 80 °C, these two samples both showed the same floriated like morphology (Fig. S1, ESI).†

With the increase of the hydrothermal temperature to 90 °C, the floriated nanostructure disappeared, but some nanobelt structures appeared among the formless particles (Fig. 4a and 4b), which indicated that the nanosheets were not stable at high

temperature. For a hydrothermal temperature of 100 °C, the morphology of $Zn_3V_2O_7(OH)_2(H_2O)_2$ completely changed. The low magnification SEM image of the as-synthesized product displays a large quantity of nanobelt nanostructures, along with a few nanoparticle (Fig. 4c). The lengths were up to several micrometers. Fig. 4d shows that the product exhibited nanobelt-like structures with a uniform width of 100–150 nm and a thickness of 30–40 nm. The surface of the nanobelt was smooth. The fine structural details of the products were further characterised by TEM. Each nanobelt had a uniform width along its entire length and the average width was about 100–150 nm (Fig. 4e), which was consistent with the SEM results. The corresponding SAED (inset in Fig. 4f) with a regular diffraction spot array revealed that each nanobelt was a single crystalline. The lattice fringes of the nanocrystalline sample can be seen from the HRTEM image (Fig. 4f) with a spacing of about 0.211 nm, corresponding to the interplanar distance of the (202) crystal plane of the hexagonal $Zn_3V_2O_7(OH)_2(H_2O)_2$. Both the HRTEM image and SAED pattern confirmed the nanobelt grew preferentially along the [202] direction. With the hydrothermal temperature further increasing to 120 or 140 °C, $Zn_3V_2O_7(OH)_2(H_2O)_2$ basically kept the nanobelt morphology (Fig. S2, ESI).†

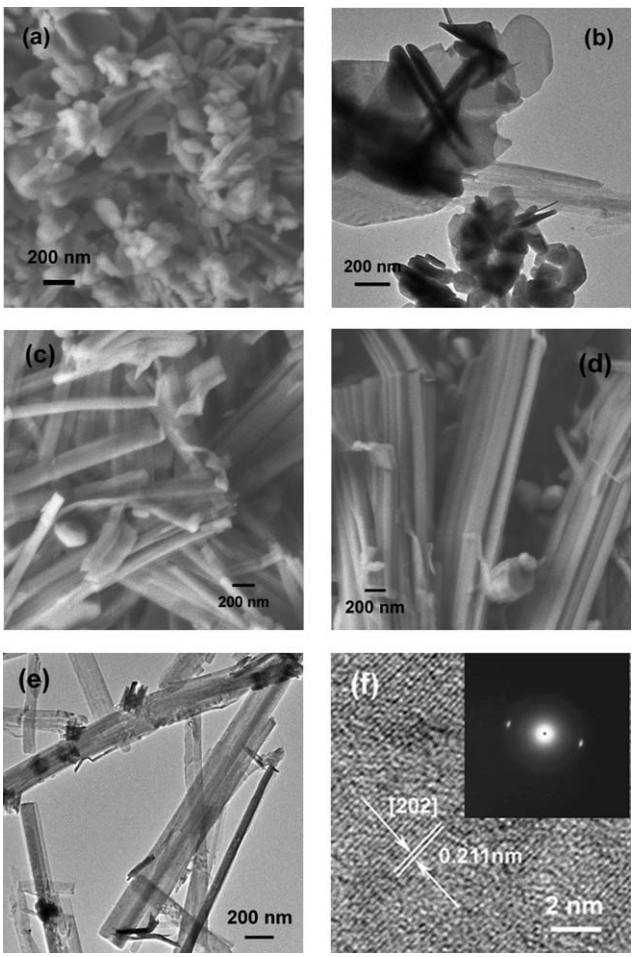

Fig. 4 SEM images (a), TEM images (b) of $Zn_3V_2O_7(OH)_2(H_2O)_2$ prepared at 90 °C. SEM images (c, d), TEM images (e), HRTEM image (f), SAED pattern (upper inset in Figure 4f) of $Zn_3V_2O_7(OH)_2(H_2O)_2$ prepared at 100 °C.

Photocatalytic activity of $Zn_3V_2O_7(OH)_2(H_2O)_2$

The photocatalytic activities of $Zn_3V_2O_7(OH)_2(H_2O)_2$ were evaluated by degradation of MB under UV light irradiation, a hazardous solution pollutant as well as a common model compound to test the photodegradation capability of photocatalysts. The blank test and photolysis of MB confirmed that MB was slightly degraded in the dark and under UV light without photocatalysts, indicating that the adsorption action and photolysis of MB can be ignored. As can be seen from the Fig. 5, the photocatalytic activities of $Zn_3V_2O_7(OH)_2(H_2O)_2$ strongly depended on the hydrothermal temperature. *Via* the first-order linear fit, the determined reaction rate constant k was 0.01526, 0.01911, 0.01433, 0.00914, 0.00156, 0.00124, and 0.00053 min^{-1}, respectively, for the samples prepared at hydrothermal temperature 60, 70, 80, 90, 100, 120 and 140 °C. The photocatalytic degradation reaction proceeded rapidly over white $Zn_3V_2O_7(OH)_2(H_2O)_2$ powders in the temperature range 60–80 °C, while almost no MB degradation was observed over the red $Zn_3V_2O_7(OH)_2(H_2O)_2$ powders in the temperature range 100–140 °C. According to the UV-vis results, lattice defects would be formed in the red $Zn_3V_2O_7(OH)_2(H_2O)_2$ powders. Hence, lattice defects in the crystal structure were considered as the main factor influencing the photocatalytic activity in the present system. In general, lattice defects may act as recombination centers for photoinduced electrons and holes, reducing the total photocatalytic activity significantly.[32] The highest activity was obtained when the hydrothermal temperature reached 70 °C. The photocatalytic activities of $Zn_3V_2O_7(OH)_2(H_2O)_2$ obtained at 60 and 80 °C were slightly smaller than that obtained at 70 °C but about 1.5 time higher than that obtained at 90 °C. The $Zn_3V_2O_7(OH)_2(H_2O)_2$ prepared at this temperature range had a similar phase structure and band gap. However, on one hand, higher temperature will lead to better nanocrystalline formation according to XRD measurement; on the other hand, the BET surface area of the samples tended to decrease slightly with an increase in hydrothermal temperature (Table 1). Generally speaking, better crystallinity and larger BET surface area will result in higher activity.[33] Hence, the $Zn_3V_2O_7(OH)_2(H_2O)_2$ obtained at 70 °C possessed optimal properties in the present work while the crystalline was improved and the BET surface area was enough to influence photocatalytic activity.

Fig. S3 (ESI)† shows the results of repeated experiments for the durability of MB degradation on $Zn_3V_2O_7(OH)_2(H_2O)_2$

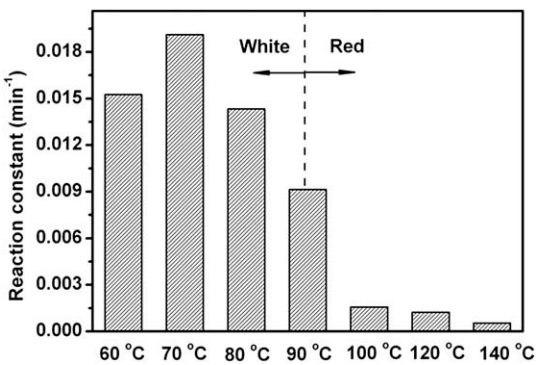

Fig. 5 Photocatalytic MB degradation under UV light irradiation over $Zn_3V_2O_7(OH)_2(H_2O)_2$ prepared at different hydrothermal temperatures.

Table 1 BET surface area of $Zn_3V_2O_7(OH)_2(H_2O)_2$ prepared at different hydrothermal temperatures

Sample	60 °C	70 °C	80 °C	90 °C
BET surface area (m^2/g)	19.0	18.1	16.0	15.3

obtained at 70 °C. MB was quickly degraded after every injection of MB, suggesting that $Zn_3V_2O_7(OH)_2(H_2O)_2$ showed relatively stable performance for MB degradation. Additionally, we evaluated the XRD pattern of the sample after the fifth run. The XRD pattern was almost similar to that of the as-prepared sample.

Formation of $Zn_3V_2O_8$

XRD patterns of $Zn_3V_2O_7(OH)_2(H_2O)_2$ obtained at different calcination temperatures are shown in Fig. 6. It illustrates that the calcination resulted in the collapse of $Zn_3V_2O_7(OH)_2(H_2O)_2$ and development of a new crystal orientation. When the reaction was carried out at 250 °C, the peaks corresponding to $Zn_3V_2O_7(OH)_2(H_2O)_2$ started to disappear and were replaced by new weak peaks. With the increase of temperature to 300 °C, several broad peaks were observed. These peaks can be readily indexed to pure orthorhombic structure $Zn_3V_2O_8$ based on the standard diffraction patterns of $Zn_3V_2O_8$ (JCPDS 34-0378). This indicated that the calcination temperature for the complete formation of $Zn_3V_2O_8$ by this method was above 300 °C. When the calcination temperature was increased to 400 or 450 °C, the XRD peaks became much sharper and more intense, because of the successful production of crystalline $Zn_3V_2O_8$. Therefore, the calcination temperature was an important optimal method for the formation of $Zn_3V_2O_8$. Moreover, the expanded diffraction peaks obviously revealed the crystalline phase was nanosized.

In order to explore the thermal stability of the hydrothermal precursor of $Zn_3V_2O_7(OH)_2(H_2O)_2$ in air, the possible gravimetric and thermal changes were investigated by TG and DTA (Fig. 7). The TG curve indicated that the increase in temperature resulted in weight loss (about 14%). The weight loss region from 40 to 400 °C was caused by the loss of adsorbed water and coordinated water. On the DTA curve three exothermic and one endothermic peaks were observed. The endothermic peak at

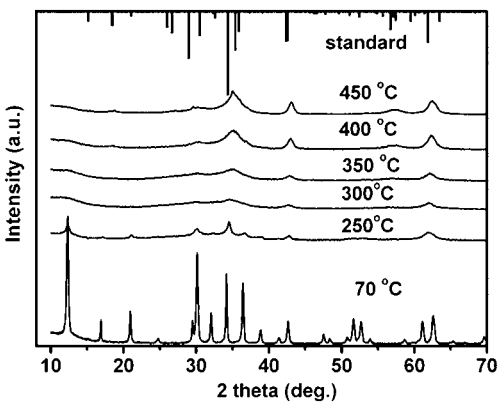

Fig. 6 XRD patterns of series $Zn_3V_2O_8$ calcined at different temperatures.

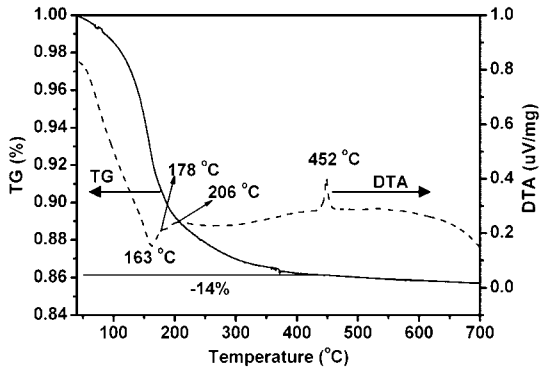

Fig. 7 TG and DTA analysis of the hydrothermal precursor of $Zn_3V_2O_7(OH)_2(H_2O)_2$ prepared at 70 °C.

163 °C was mainly attributed to the loss of the coordinated water. The exothermic peak at 178 °C was produced by the formation of $Zn_3V_2O_8$ oxide. Hence, the small peak at 206 °C resulted from the crystallization of $Zn_3V_2O_8$. Finally, the peak at 452 °C was produced by the phase transition of $Zn_3V_2O_8$. The above results suggested that $Zn_3V_2O_8$ can be formed in the temperature range 200–450 °C by calcining the corresponding $Zn_3V_2O_7(OH)_2(H_2O)_2$ precursors, which is in agreement with the XRD results.

Photophysical properties of $Zn_3V_2O_8$

UV-vis spectra of $Zn_3V_2O_8$ calcined at different temperatures are shown in Fig. 8. Based on the XRD result, a pure $Zn_3V_2O_8$ phase will be formed up to 300 °C. Above 300 °C, the absorption onset of $Zn_3V_2O_8$ is apparently red-shifted, comparing with that of $Zn_3V_2O_7(OH)_2(H_2O)_2$. The $Zn_3V_2O_8$ samples presented photoabsorption ability from the UV light region to the visible light with a wavelength shorter than 430 nm (~2.89 eV), which was in good agreement with previous reports.[21] Hence, $Zn_3V_2O_8$ held the band gap that was able to absorb visible light, implying the possibility of photocatalytic activity under visible-light irradiation.

Morphology of $Zn_3V_2O_8$

The morphology and microstructure of $Zn_3V_2O_8$ were further examined by SEM and TEM. It was found that $Zn_3V_2O_8$

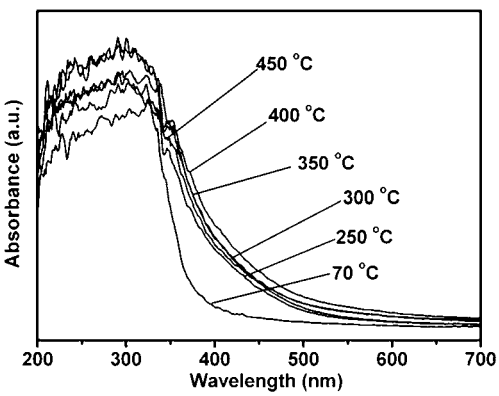

Fig. 8 UV-vis spectra of a series of $Zn_3V_2O_8$ calcined at different temperatures.

calcined at 300 °C still retained the morphology of the corresponding $Zn_3V_2O_7(OH)_2(H_2O)_2$ precursors, as shown in Fig. 9. The SEM image of calcined $Zn_3V_2O_8$ still possessed floriated nanostructures (Fig. 9a). The individual 'flower' still consisted of a large quantity of homogeneous $Zn_3V_2O_8$ nanosheets with a side length of about 500–600 nm and a thickness of about 10 nm. TEM images shown in Fig. 9b further confirmed the flowery structure was not a simple aggregation of small crystallites but was composed of nanosheet monocrystallines through self-assembly growing. Moreover, closer observation demonstrated that there were numerous porous structures within the nanosheets. As can be seen from Fig. 9c, the pore sizes within the nanosheets of the floriated $Zn_3V_2O_8$ were about 4 nm. The porous framework formed in $Zn_3V_2O_8$ could be due to the evolution of coordinated water from $Zn_3V_2O_7(OH)_2(H_2O)_2$ during the calcination. In general, porous materials exhibit a large specific surface area to increase the reaction site. Moreover, the $Zn_3V_2O_8$ laminar structure was very thick. Plenty of holes generated inside the crystalline had the opportunity to transfer to the surface and react with pollute molecules. All these characteristics of $Zn_3V_2O_8$ are beneficial for the improvement of the photocatalytic activity.[34] Energy dispersive analysis of X-rays (EDAX) was conducted for the elemental constituents of the sample, which is shown in Fig. 9d. Only Zn and V metal were found in the spectrum except for the Cu brought by the Cu grid. Quantitative results gave the atomic ratio of 22.19 : 14.22, which is close to the ideal value of 3 : 2 in $Zn_3V_2O_8$.

With the calcination temperature further increasing, nanosheet monocrystallines also can be seen, and the porous framework almost did not change, but the floriated structure started to collapse (Fig. S4, ESI).† This phenomenon was especially notable when the $Zn_3V_2O_8$ was calcined at 450 °C. High temperature treatment led to diminution of the floriated nanostructures and reduced its quality. Obviously, the sample prepared at 300 °C showed the most regular floriated nanostructures.

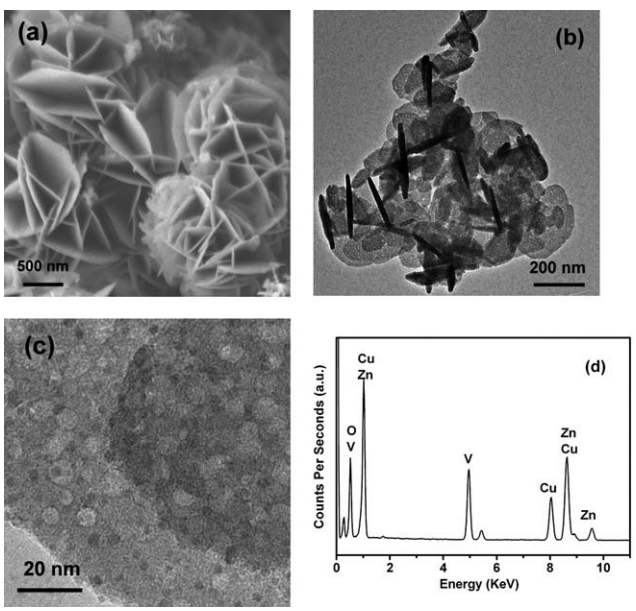

Fig. 9 SEM images (a), TEM images (b, c) and EDS spectrum (d) of $Zn_3V_2O_8$ calcined at 300 °C.

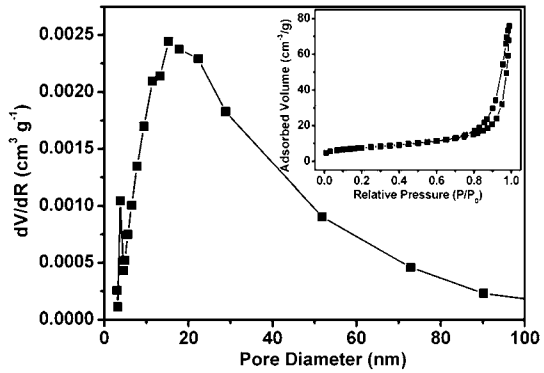

Fig. 10 N_2 adsorption-desorption isotherms (inset) and Barret-Joyner-Halenda (BJH) pore size distribution plots of the $Zn_3V_2O_8$ calcined at 300 °C.

The porous properties of floriated $Zn_3V_2O_8$ were assessed by nitrogen adsorption measurements at −196 °C. Fig. 10 shows nitrogen adsorption isotherms and pore size distributions of $Zn_3V_2O_8$ calcined at 300 °C. Clearly, two pore size distributions could be observed. One pore size distribution centered at ~4 nm, which can be attributed to the intraparticle pores in the $Zn_3V_2O_8$ nanosheets, as can be seen in TEM. Another broad peak centered at ~20 nm. Considering that the mesopores and nanosheets coexisted in the prepared sample, it would be reasonable to think that the hysteresis loop in nitrogen adsorption isotherms can be ascribed to the contribution of both intraparticle pores within the nanosheets and interparticle pores due to nanosheets accumulation.[34] Hence, the broad peak at 20 nm resulted from interparticle pores.

In the calcination temperature range 300–450 °C, an increase in temperature resulted in the broadening of interparticle pores (Fig. S5, ESI).† $Zn_3V_2O_8$ calcined at 450 °C showed the biggest pore size distribution (~30 nm). This phenomenon originated from the diminution of floriated nanostructures and reduced the quality observed in the TEM image. However, it was found that intraparticle pores within the nanosheets did not change and still retained a pore size distribution of about 4 nm. This characteristic indicated that the porous structure within the nanosheets had high stabilities during the calcination.

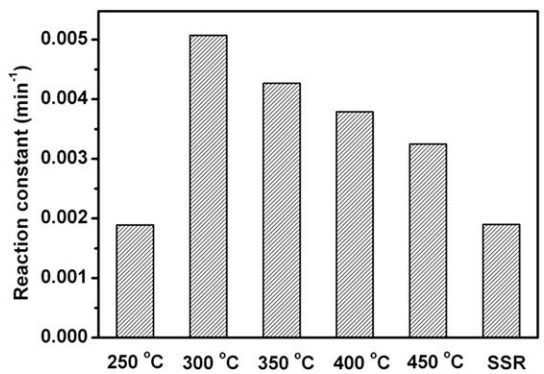

Fig. 11 Photocatalytic MB degradation under visible light irradiation (λ > 420 nm) over $Zn_3V_2O_8$ calcined at different temperatures.

Table 2 BET surface area of $Zn_3V_2O_8$ calcined at different temperatures

Sample	300 °C	350 °C	400 °C	450 °C
BET surface area (m^2/g)	28.1	27.0	25.8	23.1

Photocatalytic activity of $Zn_3V_2O_8$

Based on the DRS spectra, $Zn_3V_2O_8$ samples presented photoabsorption ability from the UV light to the visible-light region. In order to confirm visible-light-induce photocatalysis, MB degradation was carried out under visible-light irradiation (λ> 420 nm). For comparison, the MB photodegradation by $Zn_3V_2O_8$ synthesized by solid-state reaction (SSR) sample was also performed. As shown in Fig. 11, it is obvious that MB could be degraded over all the samples, and the calcination temperature had significant effect on the degradation rate. Among series samples, only the sample prepared at 250 °C showed lower activity than the SSR sample. That sample was a mixed phase with not high crystallinity, which was confirmed by XRD. Many defects could act as an electron-hole recombination center. So the photocatalytic activity was low. In the range 300–450 °C, an increase in the calcination temperature resulted in the deceleration of MB degradation. The determined reaction rate constant k was 0.00189, 0.00507, 0.00427, 0.00379, 0.00325 min^{-1}, respectively, for the samples calcined at temperatures 250, 300, 350, 400, and 450 °C. Considering the difference of the BET surface area between series samples (Table 2), the high activity of $Zn_3V_2O_8$ calcined at 300 °C was ascribed to a large surface area for adsorbing substrates to accelerate the photocatalytic degradation. In contrast, the constant k of the SSR sample was only 0.0019 min^{-1}. That meant the reaction constant of the best quality $Zn_3V_2O_8$ floriated nanostructures was about three times that of the sample prepared by the SSR method.

Fig. S6 (ESI)† shows the results of repeated experiments for the durability of MB degradation on $Zn_3V_2O_8$ calcined at 300 °C under visible-light irradiation (λ > 420 nm), suggesting that $Zn_3V_2O_8$ shows a relatively stable performance for MB degradation. We evaluated the XRD pattern of the sample after the fifth run. The XRD pattern was almost similar to that of the as-prepared sample.

In order to further understand the mineralization properties of $Zn_3V_2O_8$, the decrease of TOC in the photodegradation of MB by $Zn_3V_2O_8$ calcined at 300 °C is shown in Fig. 12. The complete degradation of the MB required 10 h. The rate of TOC reduction was slower than that of the degradation of the MB, 38% of TOC still remained in the suspension when MB was completely transformed, which suggests that the cleavage of the conjugated chromophore ring of MB resulting in the intermediates occurs during the photocatalytic process.[35] The composition of MB intermediates were detected by HPLC and further identified by LC/MS. The suggested structures of the intermediates based on the LC/MS results are shown in Fig. S7 (ESI).†

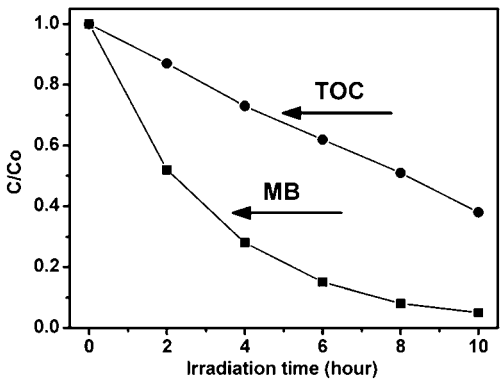

Fig. 12 Changes in MB concentration and TOC under visible light irradiation (λ > 420 nm) by $Zn_3V_2O_8$ calcined at 300 °C.

Conclusion

In summary, we have developed a facile and template-free route for the controllable synthesis of $Zn_3V_2O_7(OH)_2(H_2O)_2$ with floriated like and nanobelt nanostructures. The as-prepared floriated nanostructures were composed of 2D nanosheets (with a side length of 500 nm and a thickness of about 10 nm), which intercrossed with each other. The nanobelt nanostructures were up to several micrometers in length, 100–150 nm in width and 30–40 nm in thickness. Moreover, for the first time, we found that the $Zn_3V_2O_7(OH)_2(H_2O)_2$ had photocatalytic activity for organic pollutant degradation. Floriated $Zn_3V_2O_8$ nanostructures with pores could be achieved by subsequent heat-treatment process and showed high photocatalytic activity under visible-light irradiation. Comparing with the $Zn_3V_2O_8$ prepared by the SSR method, the reaction constant of the $Zn_3V_2O_8$ nanostructures increased about 2 times for the degradation of MB.

Acknowledgements

This work was partly supported by the National Natural Science Foundation of China (20925725 and 50972070) and National Basic Research Program of China (2007CB613303).

Reference

1 M. Hoffmann, S. Martin, M. Choi and D. Banhnemann, *Chem. Rev.*, 1995, **95**, 69.
2 X. Tao, W. Wa, T. Zhang and J. Zhao, *Angew. Chem., Int. Ed.*, 2001, **40**, 3014.
3 A. Fujishima and K. Honda, *Nature*, 1972, **238**, 37.
4 M. Addamo, V. Augugliaro, A. Dipaola, E. Garcia-Lopez, V. Loddo, G. Marci, R. Mollinari, L. Palmisano and M. Schiavello, *J. Phys. Chem. B*, 2004, **108**, 3303.
5 H. Kominami, S. Murakami, J. Kato, Y. Kera and B. Ohtani, *J. Phys. Chem. B*, 2002, **106**, 10501.
6 C. Yu, L. Zhang, Z. Zheng and J. Zhao, *Chem. Mater.*, 2003, **15**, 2280.
7 R. Asahi, T. Morikawa, T. Ohwaki, K. Aoki and Y. Taga, *Science*, 2001, **293**, 269.
8 S. Khan, M. Shahry and W. Lngler, *Science*, 2002, **297**, 2243.
9 B. Kraeutler and A. Bard, *J. Am. Chem. Soc.*, 1978, **100**, 4317.
10 H. Shanmugasundaram Sakthivel, *Angew. Chem., Int. Ed.*, 2003, **42**, 4908.
11 H. Fu, L. Zhang, S. Zhang and Y. Zhu, *J. Phys. Chem. B*, 2006, **110**, 3061.
12 Z. Zou, J. Ye, K. Sayama and H. Arakawa, *Nature*, 2001, **414**, 625.
13 H. Fu, C. Pan, W. Yao and Y. Zhu, *J. Phys. Chem. B*, 2005, **109**, 22432.
14 J. Tang, Z. Zou and J. Ye, *Angew. Chem., Int. Ed.*, 2004, **43**, 4463.
15 R. Shi, J. Lin, Y. Wang, J. Xu and Y. Zhu, *J. Phys. Chem. C*, 2010, **114**, 6472.
16 T. Kato, Z. Zou, M. Katagiri and J. Ye, *Chem. Mater.*, 2007, **19**, 198.

17 M. Oshikiri, M. Boero, J. Ye, Z. Zou and G. Kido, *J. Chem. Phys.*, 2002, **117**, 7313.
18 A. Kudo, K. Omori and H. Kato, *J. Am. Chem. Soc.*, 1999, **121**, 11459.
19 J. Yu and A. Kudo, *Adv. Funct. Mater.*, 2006, **16**, 2163.
20 J. Ye, Z. Zou, M. Oshikiri, A. Matsushita, M. Shimoda, M. Imai and T. Shishido, *Chem. Phys. Lett.*, 2002, **356**, 221.
21 D. Wang, J. Tang, Z. Zou and J. Ye, *Chem. Mater.*, 2005, **17**, 5177.
22 L. Zhang, I. Djerdj and M. Niederberger, *Adv. Mater.*, 2007, **19**, 2083.
23 C. Zhang and Y. Zhu, *Chem. Mater.*, 2005, **17**, 3537.
24 M. Gudiksen, L. Lauhon, J. Wang, D. Smith and C. Lieber, *Nature*, 2002, **415**, 617.
25 Y. Xia, P. Yang, Y. Sun, Y. Wu, B. Mayers, B. Gates, Y. Yin, F. Kim and Y. Yan, *Adv. Mater.*, 2003, **15**, 353.
26 L. Zhang, W. Wang, L. Zhou and H. Xu, *Small*, 2007, **3**, 1618.
27 Q. Zhao, Y. Xie, Z. Zhang and X. Bai, *Cryst. Growth Des.*, 2007, **7**, 153.
28 J. Lin, J. Lin and Y. Zhu, *Inorg. Chem.*, 2007, **46**, 8372.
29 A. Kudo, I. Tsuji and H. Kato, *Chem. Commun.*, 2002, 1958.
30 V. Kuznetsov and N. Serpone, *J. Phys. Chem. B*, 2006, **110**, 25203.
31 L. Zhang, L. Wang and Y. Zhu, *Adv. Funct. Mater.*, 2007, **17**, 3781.
32 T. Xu, X. Zhao and Y. Zhu, *J. Phys. Chem. B*, 2006, **110**, 25825.
33 H. Kato, K. Asakura and A. Kudo, *J. Am. Chem. Soc.*, 2003, **125**, 3082.
34 H. Lv, L. Ma, P. Zeng, D. Ke and T. Peng, *J. Mater. Chem.*, 2010, **20**, 3665.
35 H. Fu, L. Zhang, W. Yao and Y. Zhu, *Appl. Catal., B*, 2006, **66**, 100.

